

Satellite Observation of Volcanic Ash Clouds

Masami Tokuno

*Meteorological Satellite Center, Japan Meteorological Agency,
3-235 Nakakiyoto, Kiyose-shi, Tokyo 204, Japan*

(Received 7 October 1996 ; revised version accepted February 18, 1997)

Abstract

This report summarizes of the author's presentation, "Satellite Observation of Volcanic Ash Clouds", made at the Asia/Pacific Regional Workshop on Volcanic Ash Hazards, in Darwin, Australia, September 18-21, 1995. The work involved satellite monitoring of volcanic ash clouds from Mt.Bezymianny eruptions October 5-6, 1995.

The effectiveness of a series of visible and infrared imaging of GMS together with NOAA AVHRR window channel (channels 4 and 5) imaging in determining volcanic ash clouds is shown by examples, i. e., the eruptions of Mt.Sakurajima in 1985, Mt.Pinatubo in 1991, and Mt.Sheveluch in 1993.

The effectiveness of GMS-5 window channels, IR1 (10.5-11.5 μm) and IR2 (11.5-12.5 μm), in determining volcanic ash clouds similarly to NOAA AVHRR data is shown based on results calculated by a radiative transfer model and results of GMS-5 and NOAA-14 observation for the Mt.Bezymianny eruptions.

We conclude that GMS-5 data can contribute greatly improving volcanic ash cloud warning services.

1. Introduction

This report summarizes our presentation, "Satellite Observation of Volcanic Ash Clouds", made at the Asia/Pacific Regional Workshop on Volcanic Ash Hazards. Our work involved satellite monitoring of volcanic ash clouds from Mt.Bezymianny eruptions October 5-6, 1995. We focused on the practical effectiveness of satellite remote sensing in volcanic ash cloud warning services.

Section 2 briefly reviews GMS and NOAA satellite imaging in monitoring volcanic ash clouds over the Asia/Pacific region and the effectiveness of satellite observation in determining volcanic ash clouds in the Mt.Sakurajima eruptions in 1985, Mt.

Pinatubo eruptions in 1991, and Mt.Sheveluch eruptions in 1993. The effectiveness of NOAA AVHRR window channels (channels 4 (10.5-11.5 μm) and 5 (11.5-12.5 μm)) in the Mt.Sakurajima and Mt. Shevelch eruptions.

Section 3 describes the potential use of GMS-5 window channels IR1 (10.5-11.5 μm) and IR2 (11.5-12.5 μm) in determining volcanic ash clouds similarly to NOAA AVHRR data, based on a radiative transfer model compared to results from volcanic ash clouds from Mt.Bezymianny eruptions of October 5-6, 1995.

Section 4 presents results on the effectiveness of GMS data based on improved volcanic ash cloud detection and monitoring.

2 . Volcanic Eruption Clouds (VECs)

The first Japanese geostationary meteorological satellite (GMS) was launched in 1977, and, with additional satellites, subsequently provided low-resolution multispectral imaging at 3-hr intervals. These photographs revealed the movement of volcanic ash from Mt.El Chichon in 1983 (Funada and Arai, 1983) and the development and dispersal of clouds from Mt.Sakurajima in 1985 (Tokuno et al., 1989). In addition, GMS images were used to analyze the development and dispersal of clouds from 23 volcanoes (Sawada, 1987).

In March, 1987 hourly imaging became possible, and this data made it easier to analyze the development and dispersal of clouds from major volcanoes, Mt.Pinatubo 1991, Mt.Sheveluch 1993, Mt.Rabaul 1994, Mt.Klyuchevski 1994, etc..

The sections below describe satellite monitoring of VECs from three volcanoes—Mt.Sakurajima 1985, an example of a small eruption ; Mt.Pinatubo 1991, an example of a large eruption in a low latitude ; and Mt.Sheveluch 1993, an example of a large eruption at a high latitude.

2.1 Mt.Sakurajima Eruption

Mt.Sakurajima (31°34'25"N, 130°39'40"E) erupted frequently from Sep. 5 to Sep. 6, 1985, accompanied by VECs.

Visible GMS-3 images at 3-hr intervals detected the eruption of Mt.Sakurajima and traced the movement of VECs (Fig. 1). These traveled northwest away from the volcano as surface observatories reported, and falling was observed at the surface observatories in western Kyushu particularly about 300 km leeward from the volcano (Fig. 2). A comparison of the two figures shows that VEC distribution corresponds to that of falling ash, inferring that VECs contains much ash.

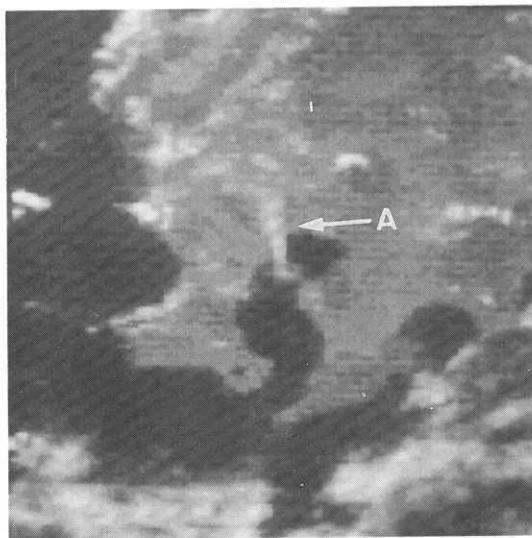
To examine the effectiveness of NOAA-9 AVHRR window channels (channels 4 and 5) for

distinguishing between volcanic ash and ice/water clouds, we studied brightness temperature differences (BTDs) e.g., BTD -0.5°C to 1.5°C corresponding to a volcanic ash cloud area and BTD 0.5°C to 1.5°C corresponding to ice/water cloud (middle cloud) south away from Kyushu (Fig. 3). A scatter diagram of BTD vs. brightness temperature (TBB) for areas A and B clearly shows the difference between volcanic ash and middle cloud (Fig. 4). As discussed in Section 3, if the cloud is semitransparent, the BTD for ice/water becomes positive and that for volcanic ash becomes negative. Positive values for BTD increase in proportion to the amount of atmospheric moisture particularly over clear areas as the BTD corresponding to about 20°C of TBB (channel 4) takes about 2 to 3°C in a clear area (Fig. 4). In addition, the IR temperature observed becomes warmer as optical cloud depth decreases because of the penetration of warmer temperature from under the surface (Fig. 4). These results prove the effectiveness of NOAA AVHRR window channels (channels 4 and 5) for distinguishing between ice/water and volcanic ash clouds from relatively small volcanic eruptions such as Mt.Sakurajima.

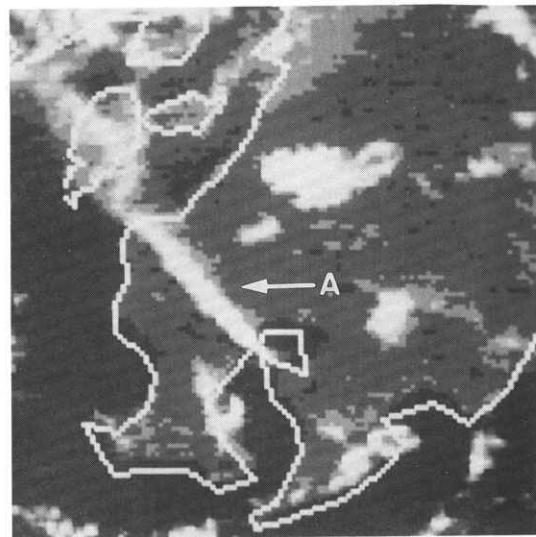
2.2 Mt.Pinatubo Eruption

This century's largest volcanic eruption occurred in the Philippines at Mt.Pinatubo (15°07'N, 120°20'E, altitude: 1745 m, June 15, 1991), and was accompanied by gigantic VECs observed at 1-hr intervals using the multispectral imaging from GMS-4.

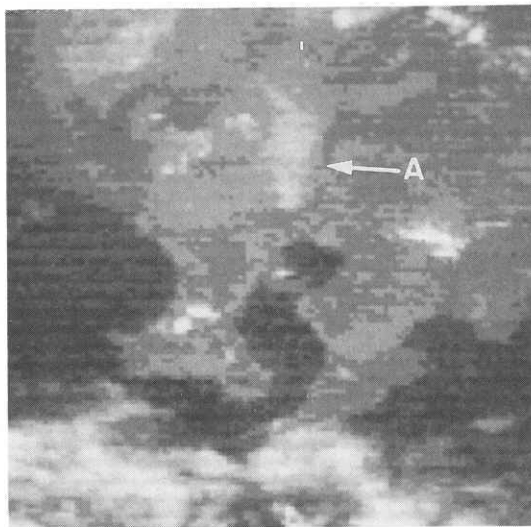
VECs (Fig. 5) in a series of VEC visible (VIS) photographs taken at 1-hr intervals from 2240UTC on June 14 to 0840UTC on June 15, 1991, are characterized by a visible gray area and disc-shaped clouds over in the center of Luzon island. The formation and dispersion of these clouds was repeatedly observed in all satellite images taken on the morning of that day. Another visible gray area



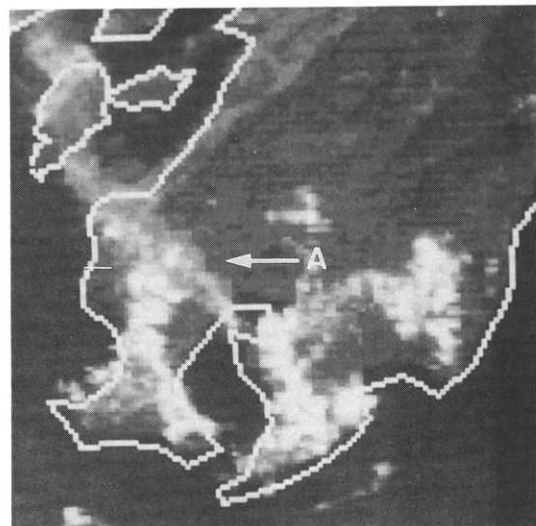
1985. 9. 5. 02:31UTC



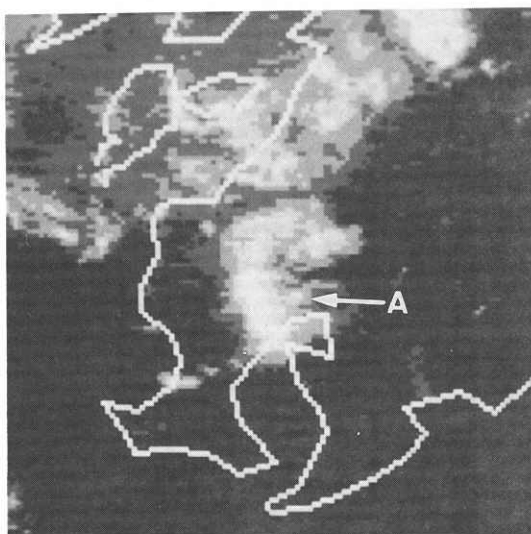
1985. 9. 5. 23:31UTC



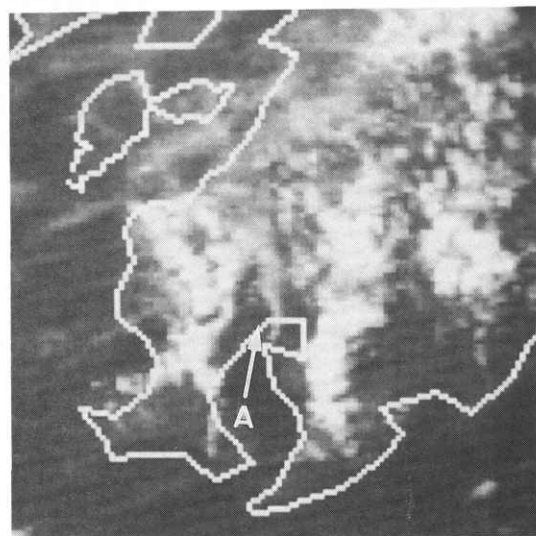
1985. 9. 5. 05:31UTC



1985. 9. 6. 02:31UTC



1985. 9. 5. 08:27UTC



1985. 9. 6. 05:31UTC

Fig. 1 GMS-3 visible images at 3-hr intervals from 0231 UTC to 0827 UTC Sep. 5, 1985 and from 2331 UTC Sep. 5 to 0531 UTC Sep. 6, 1985. 'A' indicates volcanic ash clouds from Mt. Sakurajima.

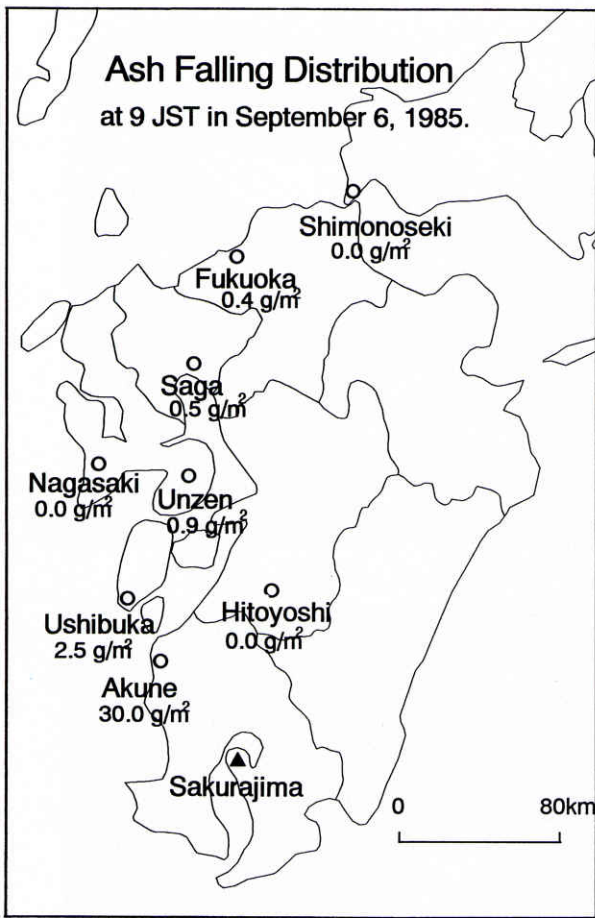


Fig. 2 The distribution of falling ash in Kyushu from Sep. 5 to Sep. 6, 1985 (from JMA News (1985)).

is shown as a fuzzy pattern dispersing west from the volcano.

A remarkable disc-shaped VEC at 0640UTC has its center nearly 20 km west of the volcano and extends up to 300 km in diameter. The largest average velocity of this extension was on the volcano's west side (47 m/s), followed by south (39 m/s), north (25 m/s), and east (22 m/s).

One hour later, the disc-shaped VEC had further expanded to 400 km in diameter. The white tops of VECs and their shadows to the east are clearly observable as they travel west away from the volcano. The largest average VEC extension velocity occurred on the volcano's east side (nearly 20 m/s), with all velocities decreasing significantly.

The last VIS image shows both a further exten-

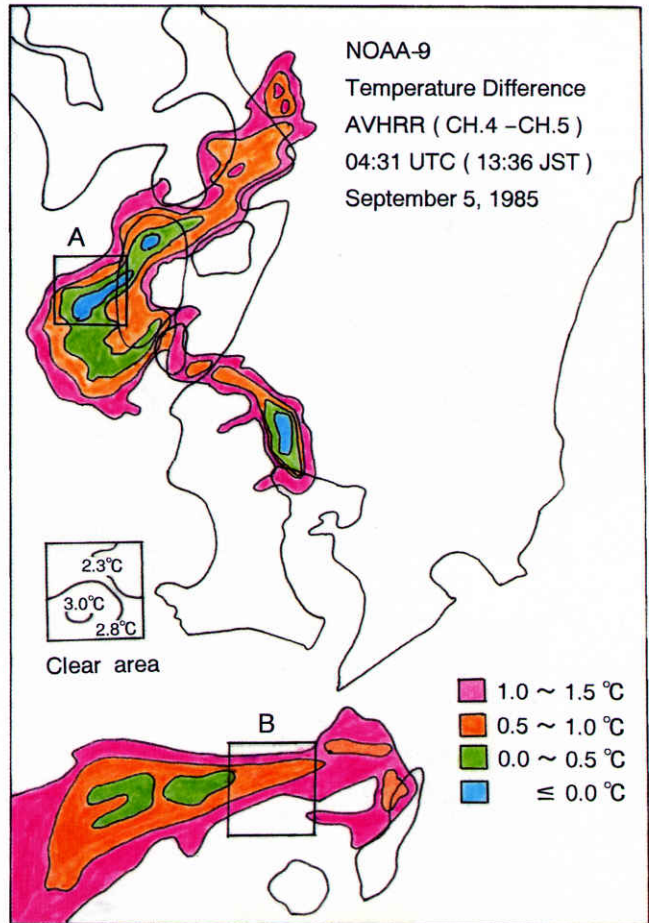


Fig. 3 NOAA-9 BTM distribution at 0436 UTC Sep. 5, 1985. 'A' represents volcanic ash cloud area and 'B' ice/water cloud area. Isothermal lines in a clear area represent BTM distribution.

sion to 600 km in diameter, especially 200 km upwind at a velocity of 15 m/s from the volcano, and westward VEC dispersion.

Hourly GMS image data thus has proved very useful in monitoring VECs.

The analysis of infrared data is described elsewhere, e.g., Tokuno (1991).

2.3 Mt. Sheveluch Eruption

Large eruptions occurred three times, at 2305UTC and 2330UTC April 21 and 1530UTC April 22, 1993, at Mt. Sheveluch (56°38'N, 161°19'E) on the Kamchatka Peninsula in Russia.

VEC development from the Mt. Sheveluch erup-

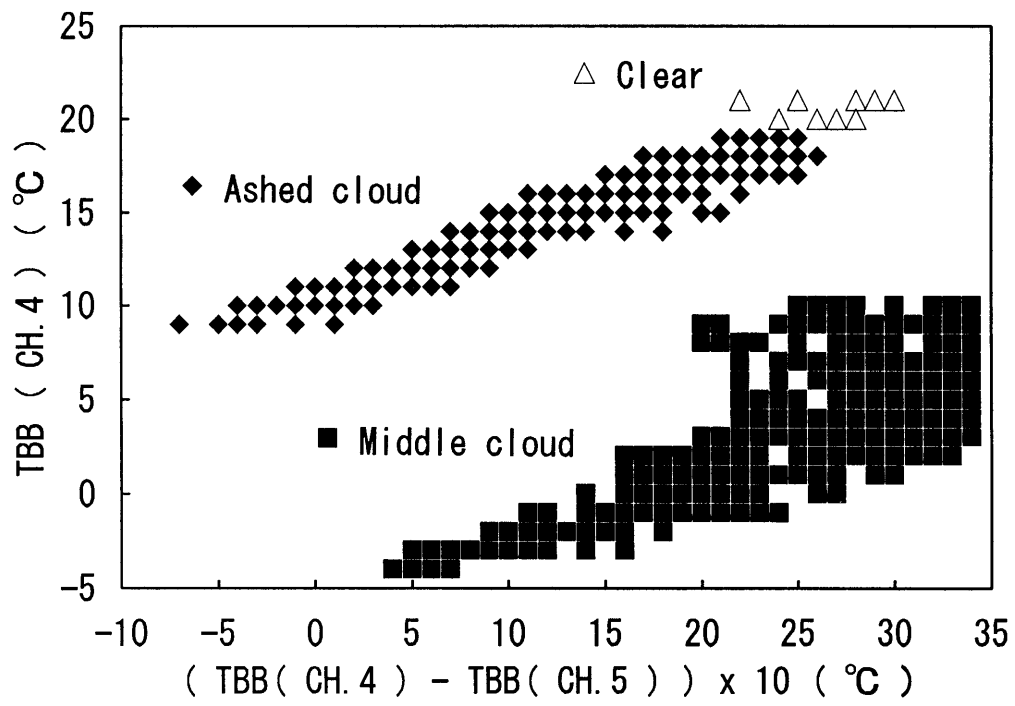
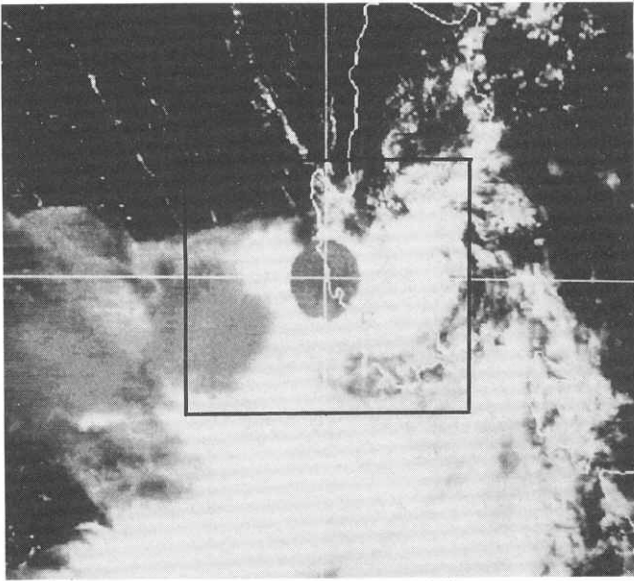
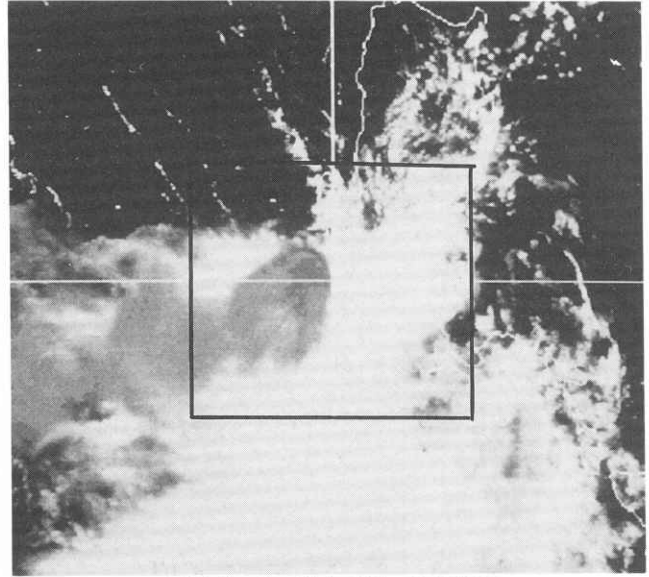


Fig. 4 Scatter diagram of BTD vs. channel 4 TBB for areas 'A' and 'B' in Fig. 3. The symbols represent individual pixel for volcanic ash cloud (◆), middle cloud (■) and clear area (△).

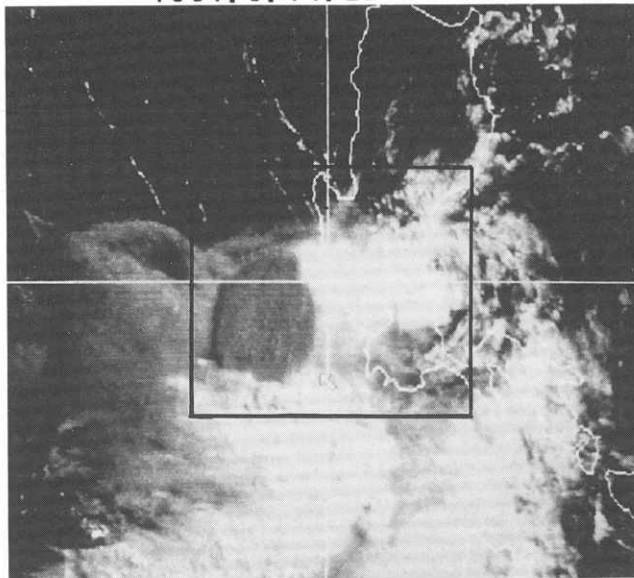
Satellite Observation of Volcanic Ash Clouds



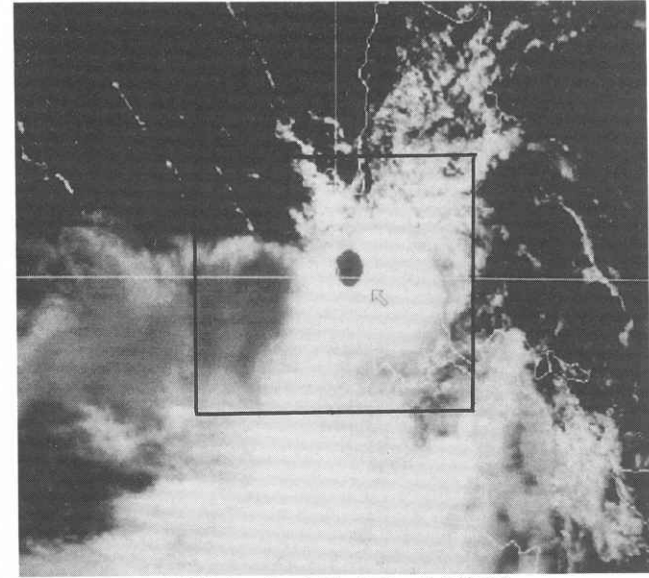
1991.6.14.22:40UTC



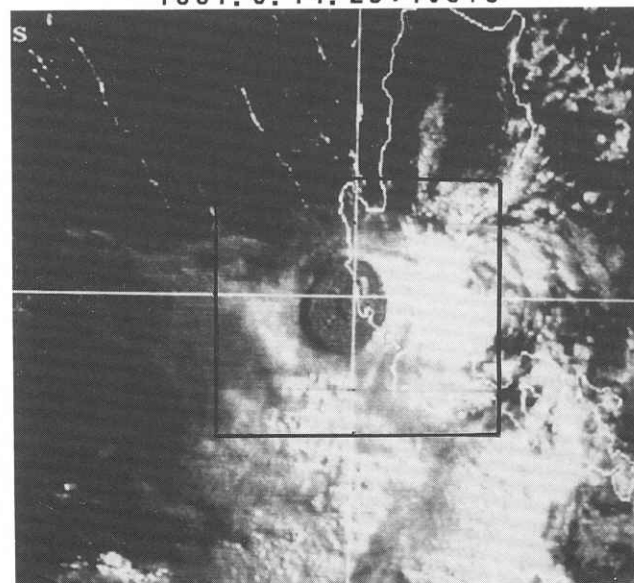
1991.6.15.01:40UTC



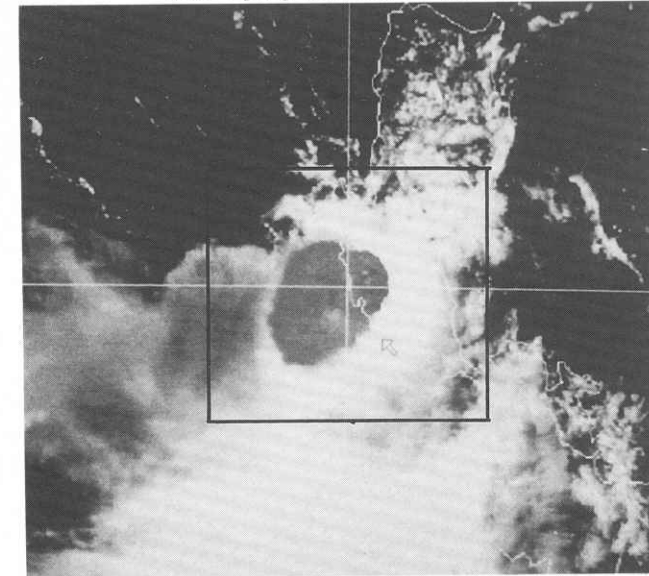
1991.6.14.23:40UTC



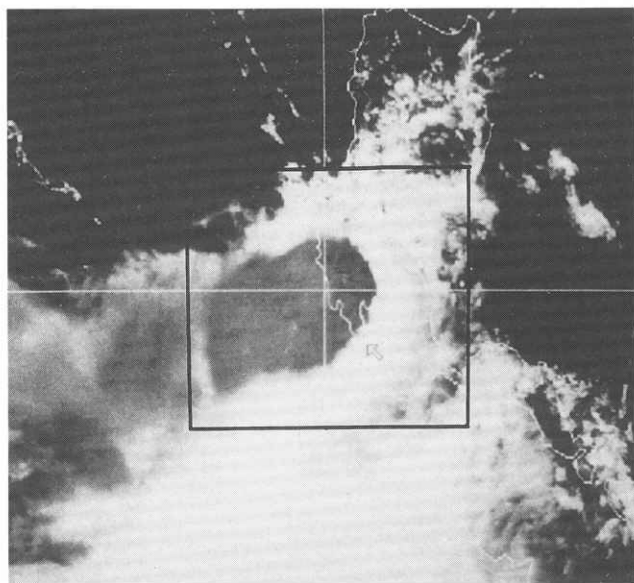
1991.6.15.02:40UTC



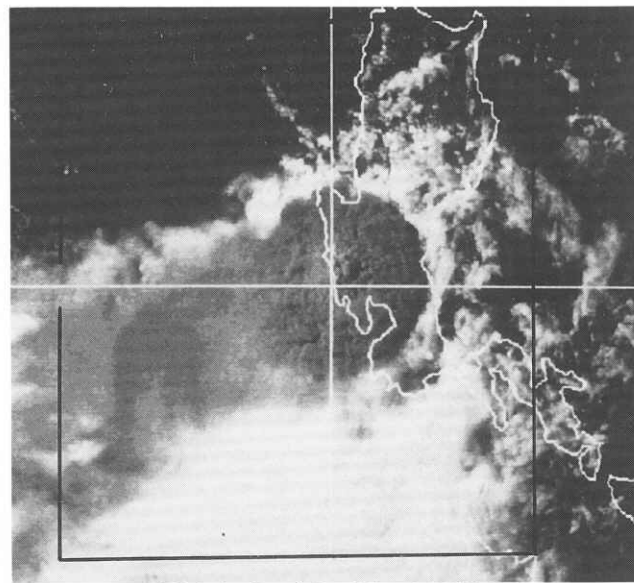
1991.6.15.00:40UTC



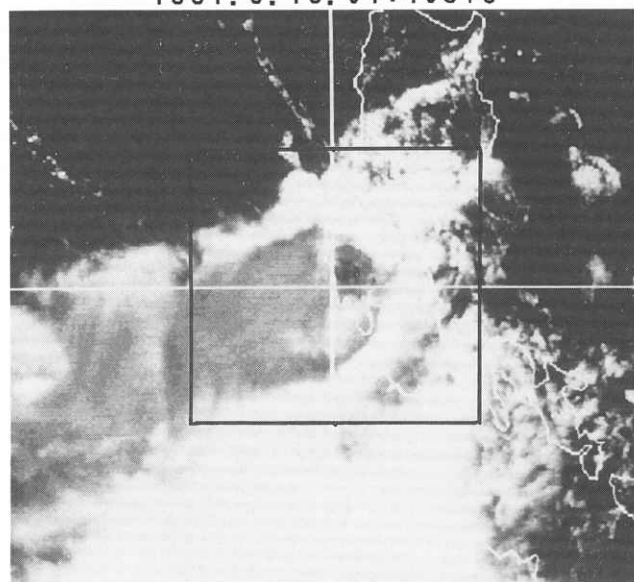
1991.6.15.03:40UTC



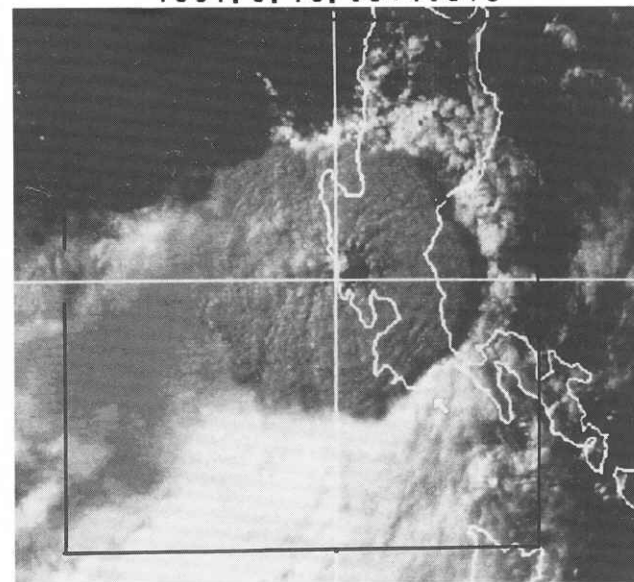
1991. 6. 15. 04:40UTC



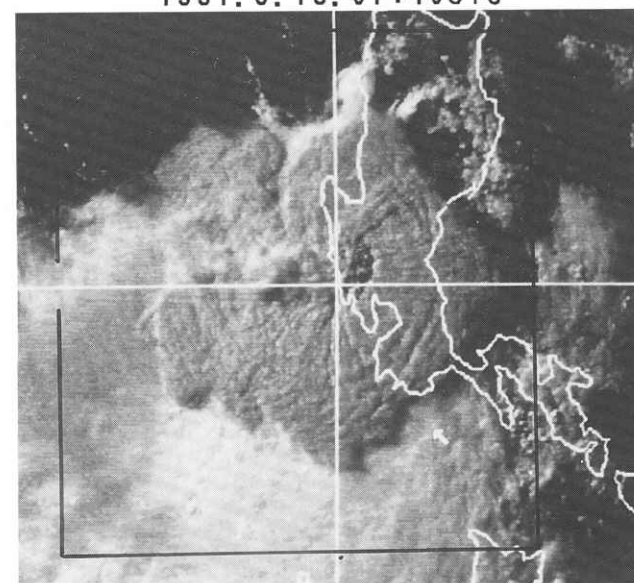
1991. 6. 15. 06:40UTC



1991. 6. 15. 05:40UTC



1991. 6. 15. 07:40UTC



1991. 6. 15. 08:40UTC

Fig. 5 A series of GMS-4 visible photographs of the Pinatubo eruption cloud taken at 1-hr intervals from 2240 UTC on June 14 to 0840 UTC on June 15, 1991.

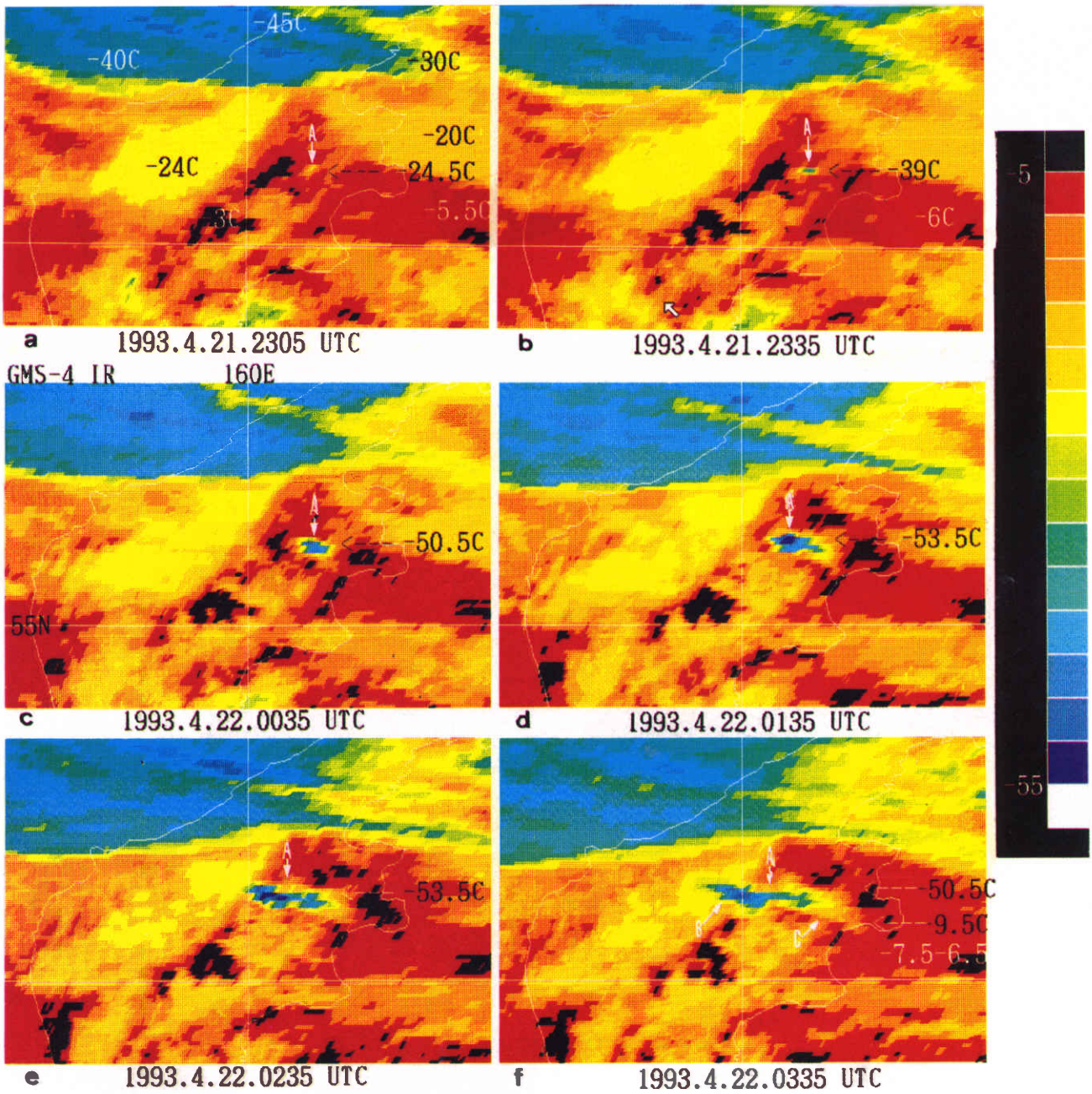


Fig. 6 A series of GMS-4 IR pseudocolor images from 2305 UTC April 21 to 0335 UTC April 22, 1993. Temperatures are indicated by the color scale on the right side. 'A' indicates VECs from Mt. Shiveluch. 'B' and 'C' respectively indicates the colder part (-51 to -35°C) and the warmer part (-35 to -10°C) of the VECs (A).

tions at 2305UTC and 2330UTC April 21, 1993, was observed in a series of GMS-4 hourly infrared images (Fig. 6). The area of VECs (A) was characterized as having the lowest temperature, -39°C , which contrasted with warmer land areas, at 00UTC April 22 (Fig. 6 (b)).

Two hours later (Fig. 6 (d) at 02UTC), the volcano's activity is considered to have continued based on the fact that the lowest temperature of the area further decreased (-53.5°C), as the area extended. The maximum VEC altitude was estimated at about 300 hPa (about 9 km) at 02UTC from infrared data and meteorological observations, if VECs are assumed to be a black body. It is generally difficult, however, to estimate the VEC altitude in the lee area from infrared data because the temperature in the lee area is higher than at the origin because of the penetration of warmer temperature from under the surface. To make up for this, it is useful to estimate VEC altitude from VEC movement based on a vertical wind profile.

The colder parts of the VECs (A) (Fig. 6 (f), B, -51 to -35°C) was dispersed west and southwest at the speed of 10 to 15 kt, while the warmer part (Fig. 6 (f), C, -35 to -10°C) was dispersed southeast at 10 to 15 kt. It is assumed that colder VEC flows correspond to air flows at 300 hPa and warmer flows to those at 100 hPa using upper weather charts. This confirms that VECs reached a height of about 8 km (nearly 350 hPa) at 2305UTC April 21 and then of about 17 km (nearly 100 hPa) (e-mail communication, Kamchatka Volcanic Eruptions Response Team (KVERT)).

Hourly observations lasted until 10UTC April 22, when VECs became too thin to be traced from infrared images.

VEC development from the Mt. Sheveluch eruption at 1530UTC April 22, 1993, was also observed in a series of GMS-4 hourly infrared images. VEC dispersion about 100 km wide extended to about 250 km south-southwest of the volcano. Its temperature

was -20°C according to the infrared image, indicating its altitude is 700 hPa.

GMS-4 hourly infrared image observations were continued until 00UTC April 25, when the vicinity of Mt. Sheveluch was covered with high clouds.

The GMS-4 infrared image at 22UTC April 23 showed that VECs with a maximum temperature of -20°C (altitude: about 700 hPa) moved indistinctly south at 10 to 15 kt, but VEC dispersion west was probably blocked by the mountains.

Effective information on VECs was received from NOAA-12 twice, at 22UTC April 22 and at 09UTC April 24.

A BTM image of AVHRR (channels 4 and 5) at 22UTC April 22 (Fig. 7) shows a smaller temperature difference (0.2 to 0.4°C) in the area indicated by 'A' than that (0.5 to 1.5°C) in the surrounding area off the south edge of the Kamchatka Peninsula. 'A' presumably contains a large amount of ash.

The vicinity of Mt. Sheveluch can be delineated as an area with a negative BTM (-1 to -3°C) from the BTM image at 09UTC April 24 (Fig. 8). This suggests that the vicinity of Mt. Sheveluch is covered with falling ash.

Findings from trial monitoring above showed that both GMS-4 hourly infrared images and BTM images are useful for delineating VECs.

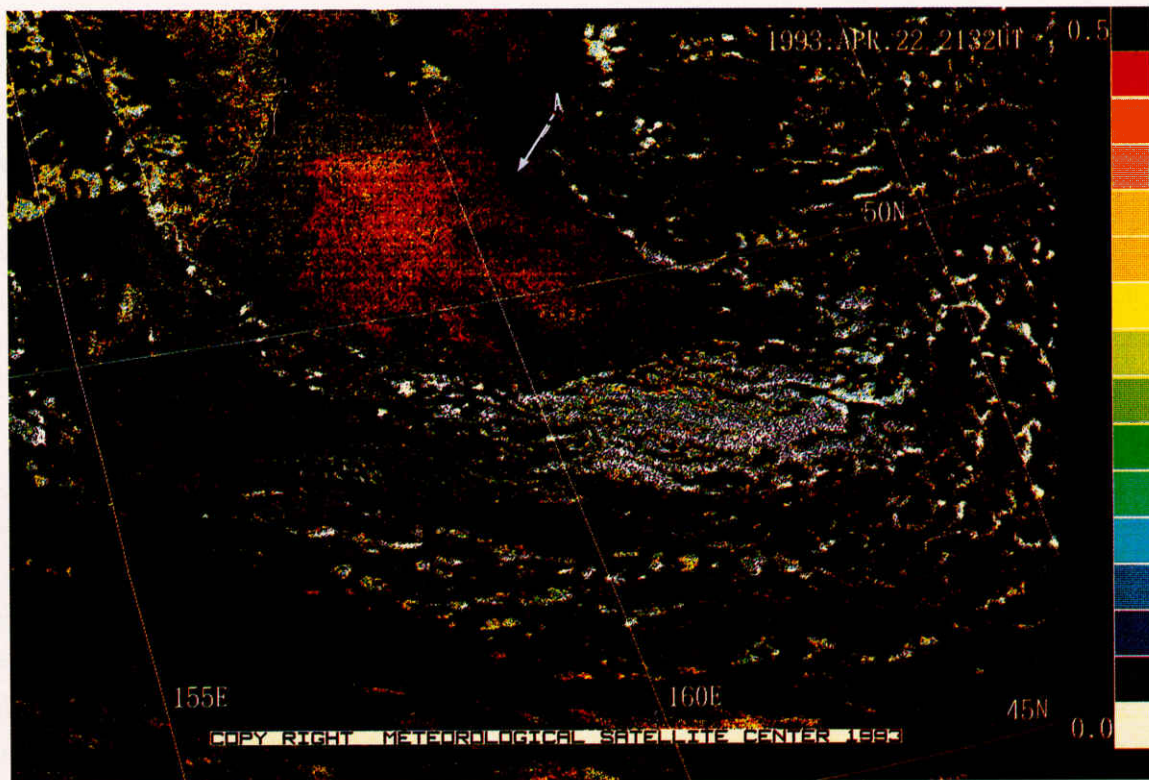


Fig. 7 BTD image of AVHRR at 22 UTC April 22, 1993. An area with a smaller BTD (0°C to 0.5°C) is colored.

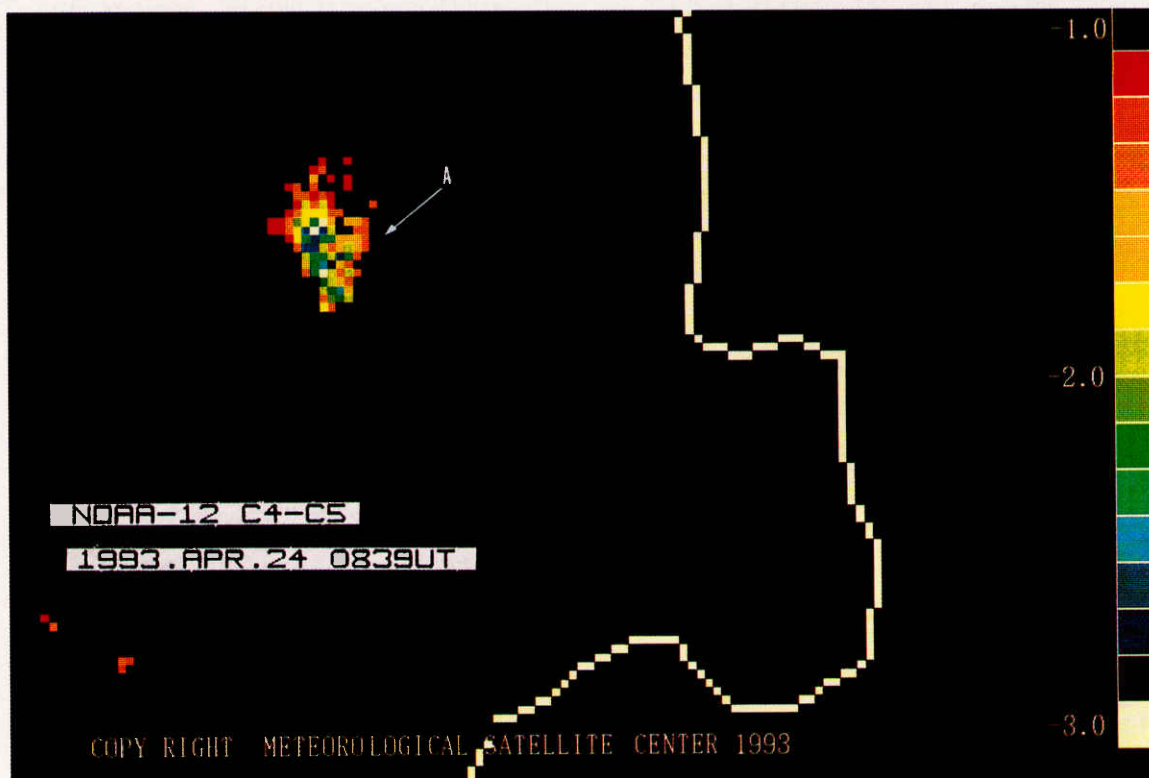


Fig. 8 BTD image of AVHRR at 09 UTC April 24, 1993. An area with a negative BTD (-1°C to -3°C) is colored.

3. GMS-5 Window Channel (IR1 and IR2) Potential

A Japanese GMS-5 geostationary satellite was launched in March 1995 and became operational in June 1995. This satellite had one visible and three infrared sensors (IR1: 10.5-11.5 μm , IR2: 11.5-12.5 μm , IR3: 6.5-7.0 μm). The two window channels, IR1 and IR2, are operated at wavelengths similar to NOAA AVHRR window channels (channels 4 and 5), which have been successfully used to distinguish volcanic ash clouds from water/ice clouds, e.g., Prata (1989) and Potts (1993). Some overlap occurs, however, in response functions for GMS-5 window channels, IR1 and IR2. We therefore studied the GMS-5 window channel potential for distinguishing volcanic ash clouds based on a radiative transfer model. We also compared calculated results with results from the Mt. Bezymianny eruptions October 5-6, 1995.

3.1 Radiative Transfer Model

If no ice/water clouds occur between the surface and overlying cloud, e. g., volcanic ash cloud, the monochromatic upwelling thermal radiance observed by the satellite sensor is expressed as

$$B_{e,\nu}(\mu) = B_{s,\nu}e^{-\tau_\nu/\mu} + \int_0^\tau e^{-\tau'/\mu} S(\tau') \frac{d\tau'}{\mu} \quad (1)$$

where ν is the wavenumber, $B_{e,\nu}$ is observed radiance, $B_{s,\nu}$ is radiance emitted from the surface, τ_ν is the cloud optical depth at wavenumber ν , and μ is the cosine of the viewing angle. The source function $S(\tau')$ is at the optical depth τ' in the cloud.

Based on a few assumption $S(\tau')$ is approximated by a two-stream source function and the cloud is isothermal, Eq. (1) becomes Eq. (2) by applying a technique developed by Ackerman et al. (1988).

$$B_{e,\nu}(\mu) = B_{s,\nu}e^{-\tau_\nu/\mu} + B_{c,\nu}(1 - e^{-\tau_\nu/\mu}) + B_{s,\nu}\delta_s(\mu, \tau_\nu) - B_{c,\nu}\delta_c(\mu, \tau_\nu) \quad (2)$$

where $B_{c,\nu}$ is the radiance of a black body at the

cloud temperature at wavenumber ν . The coefficients of the last two terms are written as

$$\delta_s = \frac{f^- - \Gamma^2 f^+}{2D} \quad (3)$$

$$\delta_c = (1 - \Gamma e^{-\lambda\tau_\nu}) \cdot \frac{(f^- + e^{\lambda\tau_\nu} \Gamma f^+)}{2D} \quad (4)$$

where

$$\left. \begin{aligned} \lambda &= 2(1-\gamma)^{\frac{1}{2}} \\ \gamma &= \tilde{\omega}_\nu(1-g_\nu) \\ D &= e^{\lambda\tau_\nu} - \Gamma^2 e^{-\lambda\tau_\nu} \\ \Gamma &= (2-\lambda)/(2+\lambda) \\ f^- &= \frac{(2-\lambda)}{(1-\mu\lambda)} \cdot (1 - e^{-(1-\mu\lambda)\tau_\nu/\mu}) \\ f^+ &= \frac{(2+\lambda)}{(1+\mu\lambda)} \cdot (1 - e^{-(1+\mu\lambda)\tau_\nu/\mu}) \end{aligned} \right\} \quad (5)$$

Here, $\tilde{\omega}_\nu$ is the single-scattering albedo and g_ν the asymmetry factor of the cloud layer.

Spaceborne satellite sensors are designed to measure radiance with some wavenumber range $\nu_1 < \nu < \nu_2$, not monochromatic radiances. The observed response-weighted radiance by the sensor of the satellite is therefore expressed as

$$I_{e,i}(\mu) = \int_{\nu_1}^{\nu_2} \hat{\Phi}_i(\nu) B_{e,\nu}(\mu) d\nu \quad (6)$$

where $\hat{\Phi}_i(\nu)$ is the normalized spectral response-function for channel i . The normalized response functions for the two GMS-5 thermal channels, 1 and 2, and the two NOAA-12 and NOAA-14 AVHRR thermal channels, 4 and 5, are shown in Fig. 9.

3.2 Mie Calculation

To obtain the theoretical radiance defined in Eq.(2), optical cloud properties cloud are required. In this study, we assumed cloud particles are spherical, so the Mie theory can be used to calculate the efficiency factor for extinction, scattering, or absorption; asymmetric parameter; and single-scattering albedo for known refractive indices. These optical properties are calculated in the following equations:

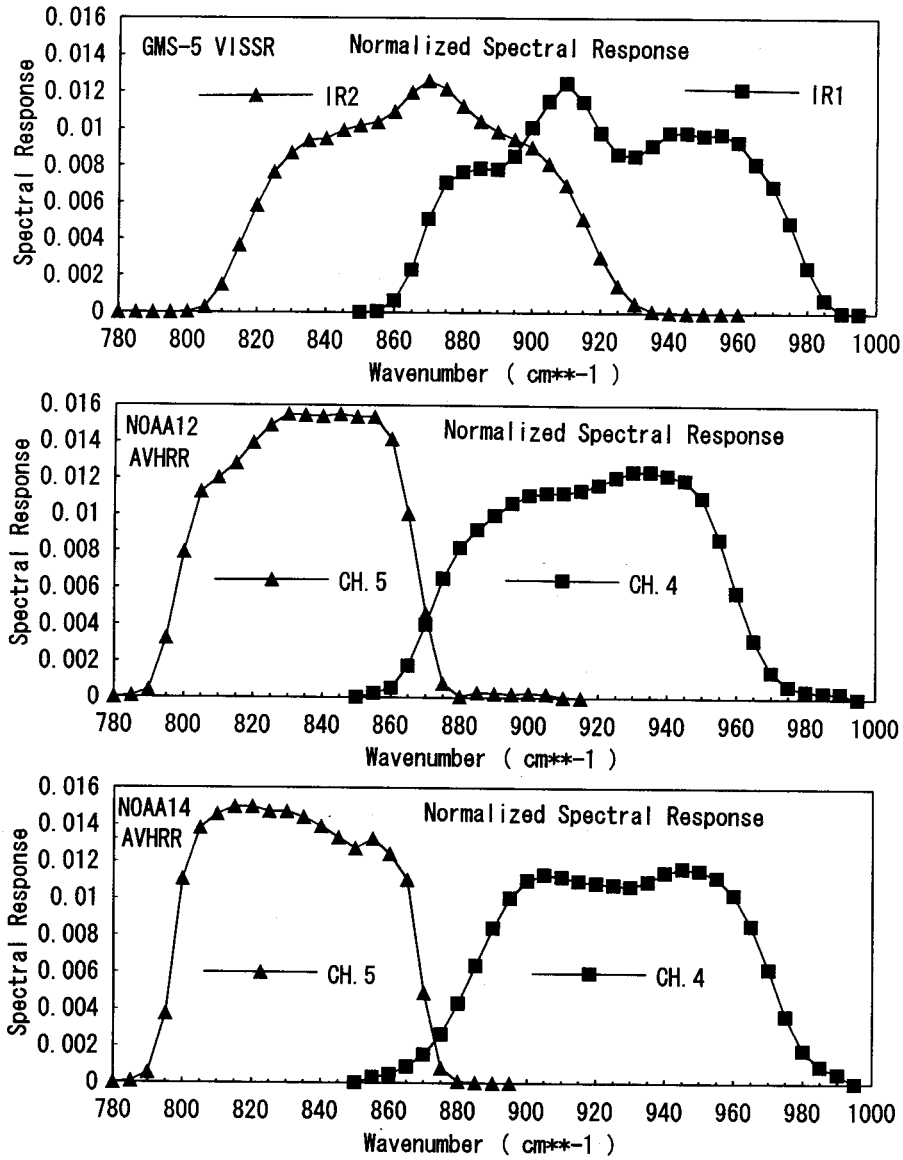


Fig. 9 Normalized spectral response-functions for the two thermal channels, 1 and 2, and the two NOAA-12 and NOAA-14 AVHRR thermal channels, 4 and 5. Spectral response at intervals of 5cm^{-1} is indicated by the symbols (\blacktriangle and \blacksquare).

Efficiency factors :

$$\bar{Q}_f = \frac{\int_0^\infty \pi r^2 Q_f(2\pi r/\lambda, m) \frac{dn(r)}{dr} dr}{\int_0^\infty \pi r^2 \frac{dn(r)}{dr} dr} \quad (7)$$

where Q_f is the Mie efficiency factor for extinction, scattering, or absorption ; $n(r)$ is the size distribution of particles with radius r in the units of number of particles per unit volume ; m is refractive indices ; and λ is wavelength.

Extinction, absorption, and scattering efficiencies

are related by

$$\bar{Q}_{ext} = \bar{Q}_{abs} + \bar{Q}_{sca} \quad (8)$$

The single scattering albedo is

$$\bar{\omega} = \bar{Q}_{sca} / \bar{Q}_{ext} \quad (9)$$

The asymmetry parameter is

$$\bar{g} = \frac{\int_0^\infty \pi r^2 Q_{sca} g(2\pi r/\lambda, m) \frac{dn(r)}{dr} dr}{\int_0^\infty \pi r^2 Q_{sca} \frac{dn(r)}{dr} dr} \quad (10)$$

where g is asymmetric parameter for a single

particle and Q_{sca} is the Mie efficiency factor for scattering.

It is assumed that particle size distribution, $n(r)$, is the modified- γ size distribution used by Prata and Barton (1994). That is, size distribution is given by

$$dn(r)/dr = (Nb^7/6!) r^6 e^{-br} \quad (11)$$

where r_0 is the mean particle radius, N is the total number of particles per unit volume, and $b = 6/r_0$.

Optical cloud thickness is calculated from the size distribution, extinction efficiency, and geometrical thickness of the cloud. These are related by

$$\tau_c = \bar{Q}_{\text{ext}} L \int_0^\infty \pi r^2 \frac{dn(r)}{dr} dr \quad (12)$$

where L is the geometrical thickness.

The above scattering parameters required for radiative transfer calculation are obtained using subroutines for computing parameters of the electromagnetic radiation scattered by a sphere developed by J.V. Dave (1968).

Fig. 10 shows the refractive indices of quartz, volcanic dust, ice, and water in the wavelength region (10–13 μm) obtained from Takashima and Masuda (1987) based on data by Spitzer and Kleinman (1961), Volz (1983), Warren (1984), and Irvine and Pollack (1967).

The modified- γ size distribution is used for calculations with a mean particle radius of 2, 3, and 5 μm . Fig. 11 shows some results of calculations for $r_0 = 3 \mu\text{m}$ and $N = 100 \text{ cm}^{-3}$, indicating that volcanic substances (quartz and dust) have an extinction larger than ice and water and that extinction decreases with wavelengths 11.5 μm and 12 μm . For water and ice the extinction increases with wavelength in this region.

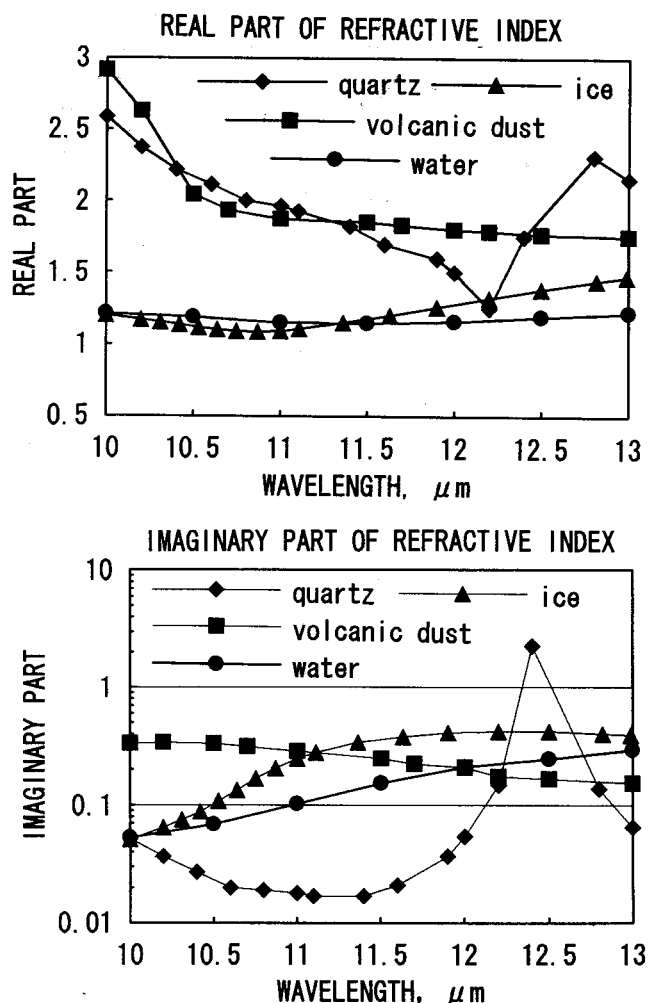


Fig. 10 Real part (upper) and imaginary part (lower) of the refractive indices of quartz (\blacklozenge), volcanic dust (\blacksquare), ice (\blacktriangle), and water (\bullet) in the wavelength region (10–13 μm) obtained from Takashima and Masuda (1987) based on data by Spitzer and Kleinman (1961), Volz (1983), Warren (1984), and Irvine and Pollack (1967),

3.3 Model Calculation

Calculation of radiance observed radiance by the satellite in the model was as follows, based on a few assumptions: (1) the vertical profile in the atmosphere is midlatitude summer/winter atmospheric model (Knelzys, 1983), (2) the cloud base height is 10 km over the surface and the geometrical cloud thickness is 1 km, (3) the satellite view angle is 180 deg., and (4) the lowest layer of the

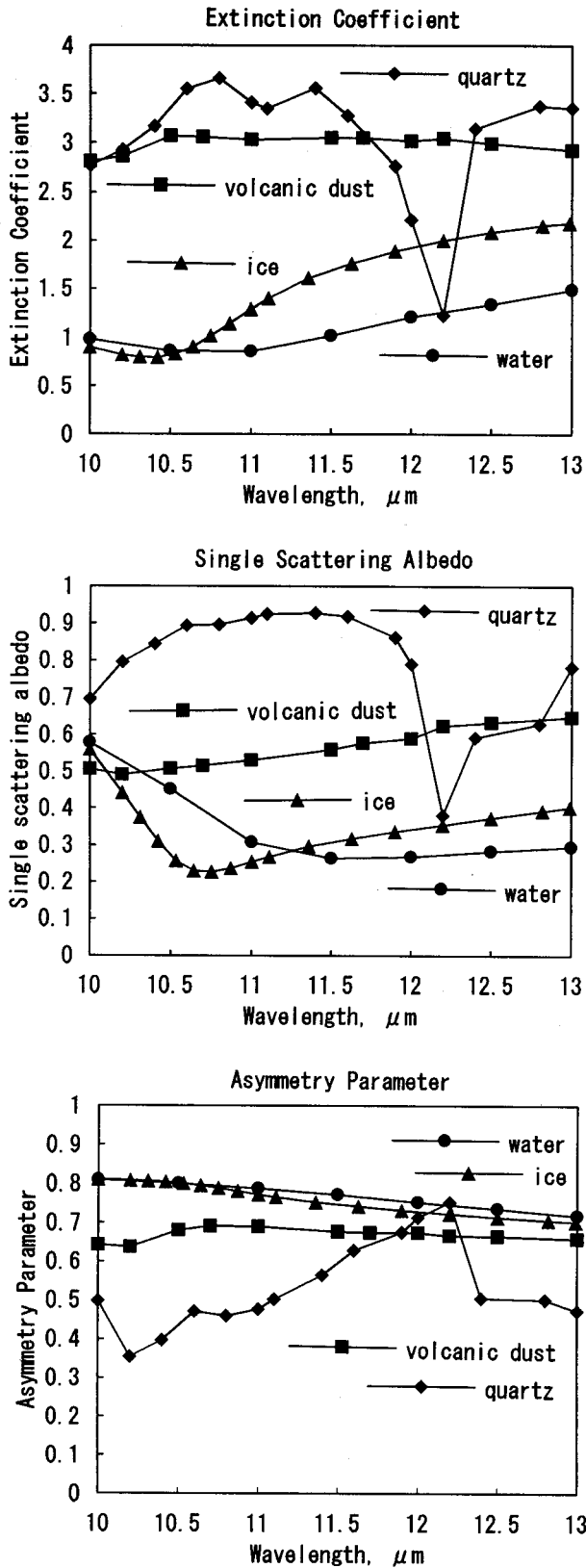


Fig. 11 Extinction efficiency factor Q_{ext} , asymmetry parameter g and single scattering albedo $\bar{\omega}$ for quartz (◆), volcanic dust (■), ice (▲) and water (●) as a function of wavelength. The modified- γ size distribution is used with $r_0 = 3\mu\text{m}$.

atmospheric model is used instead of the surface of the earth.

- 1) The values of scattering parameters in GMS-5 and NOAA-12 wavenumbers are given by interpolating the values of scattering parameters calculated in Session 3.2.
- 2) The optical cloud thickness is varied from 0 to 9 by changing the total number of particles per unit of volume.
- 3) Satellite-observed monochromatic radiances are calculated at interval 5cm^{-1} in the region of GMS-5 and NOAA-12 wavenumbers using Eq. (2).
- 4) Satellite-observed radiances for each channel are calculated by combining the response function (Fig. 9) with satellite-observed monochromatic radiances calculated in term (3), using Eq. (6).
- 5) Satellite-observed radiance is converted to brightness temperature using both the spectral response characteristics of the radiometer and the Plank function. The BTD between infrared window channels is then calculated.

We simulated temperature pairs, BTD of GMS-5 or NOAA-12 AVHRR and IR-1 temperature of GMS-5 or channel 4 temperature of NOAA-12 AVHRR as a function of mean particle radius (2, 3, or 5 μm) and the optical depth (0-9) for quartz, volcanic dust, ice and water in a mid-latitude summer atmospheric model (Figs. 12-15).

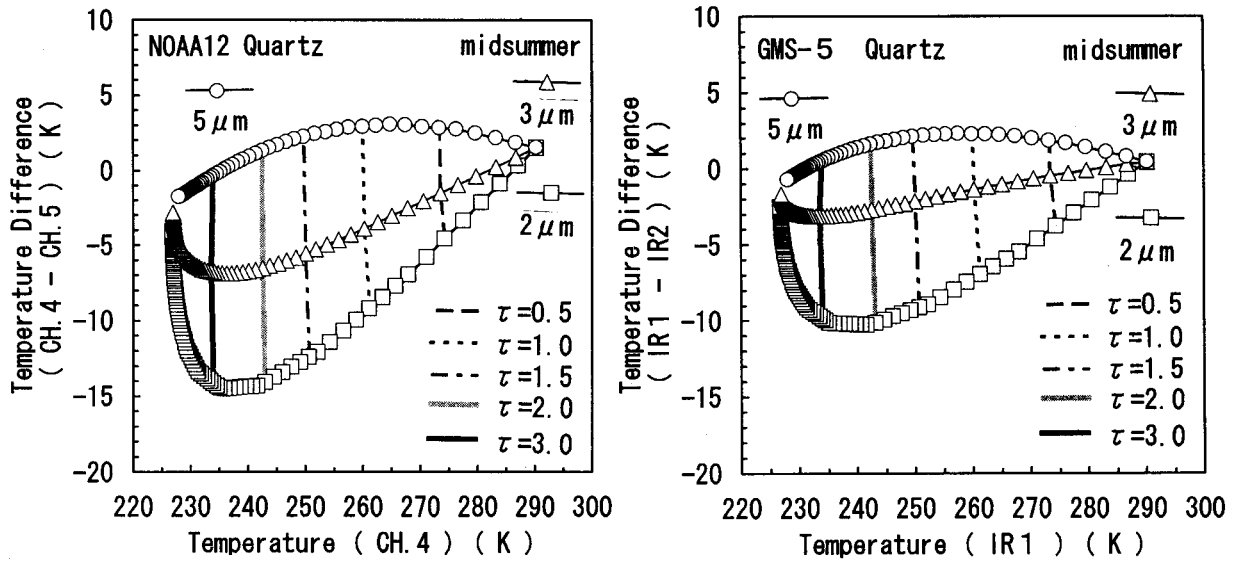


Fig. 12 Simulated temperature pairs, BTD of GMS-5 or NOAA-12 AVHRR and IR-1 temperature of GMS-5 or channel 4 temperature of NOAA-12 AVHRR as a function of mean particle radius (2,3, or $5\mu\text{m}$) and optical depth (0--9) for quartz in the mid-summer atmospheric model. The near horizontal curves represent different mean particle radii, and the near vertical curves the dependence of optical depth at IR-1 or channel 4 with particle radius.

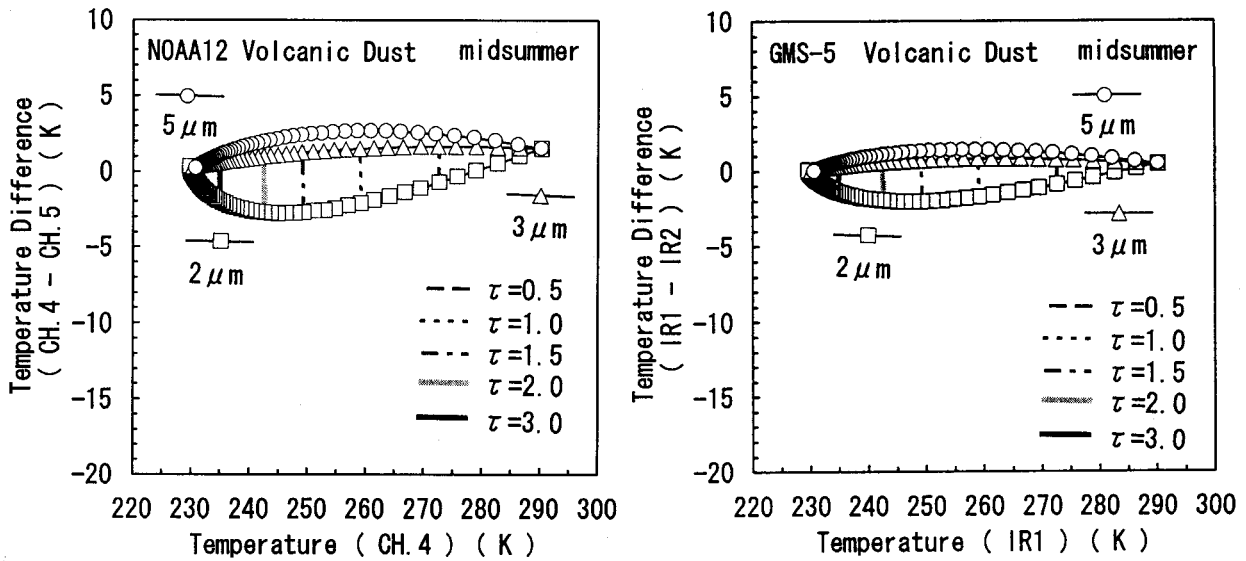


Fig. 13 Same as Fig. 12 except for volcanic dust.

As expected, for quartz, the negative BTD value is greatest in a mean particle radius of $2\mu\text{m}$, followed by $3\mu\text{m}$ and $5\mu\text{m}$. For small or large optical depth, BTD becomes small. As mean particle radius gets larger, negative BTD gradually decreases and becomes positive value. This tendency is seen in

volcanic dust, with the value for volcanic dust being smaller than that in quartz.

In the case ice and water as shown (Section 3.2), the tendency forward extinction is reverse that in quartz and volcanic dust, so the BTD tendency is reverse that of quartz and volcanic dust, i. e., the

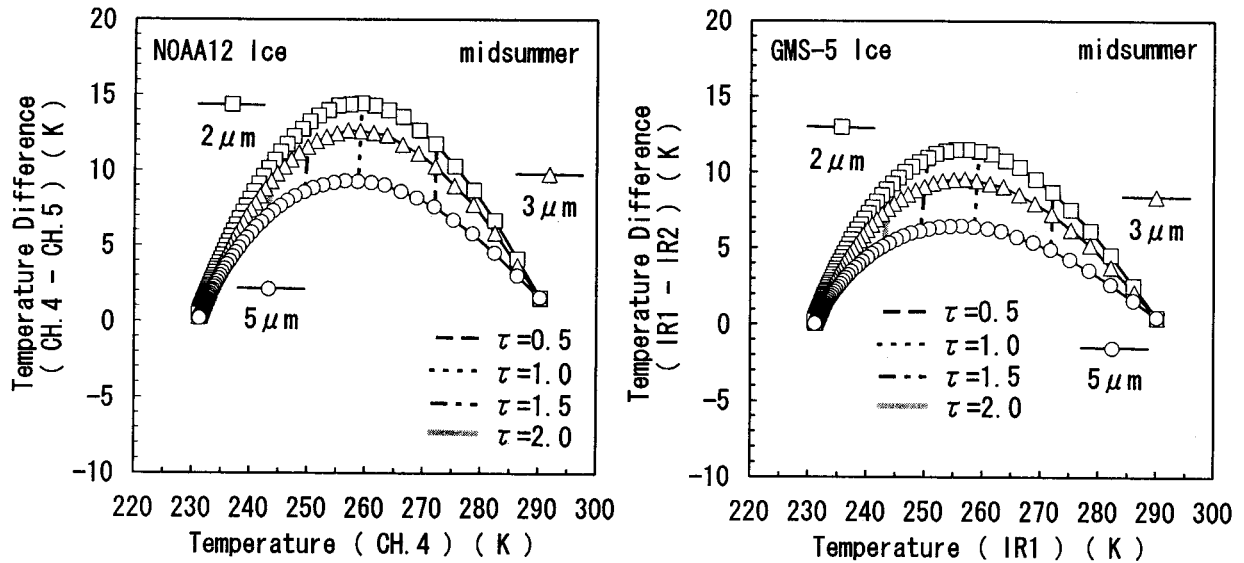


Fig. 14 Same as Fig. 12 except for ice.

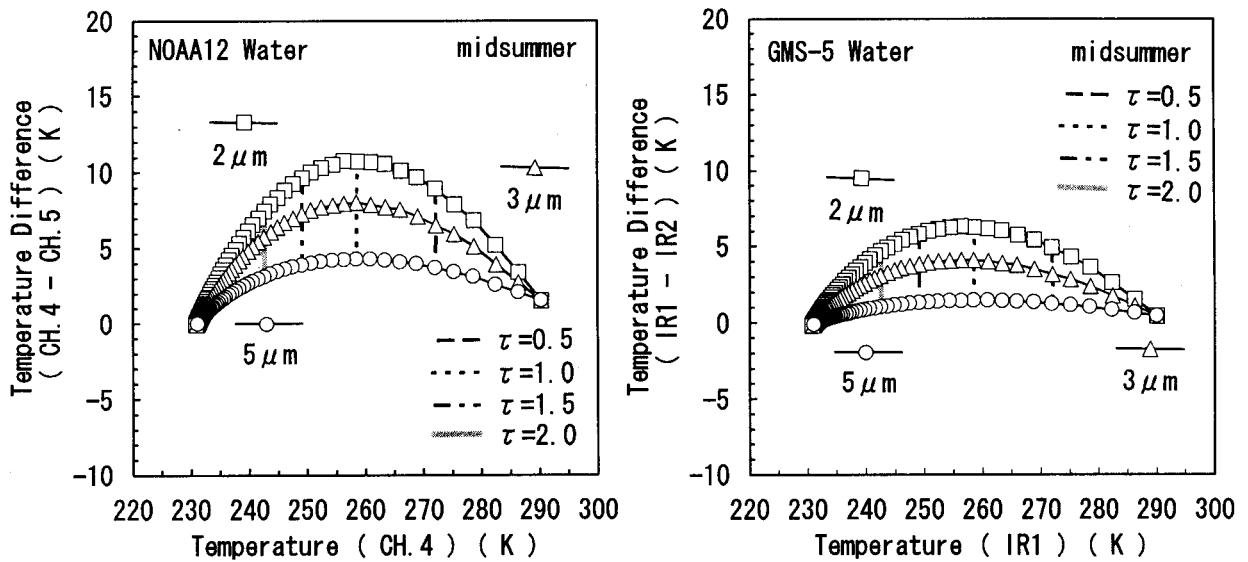


Fig. 15 Same as Fig. 12 except for water.

positive BTD value is greatest at a mean particle radius of $2\mu\text{m}$, followed by $3\mu\text{m}$ and $5\mu\text{m}$.

To investigate the effect of vertical profile in the atmosphere on BTD, the same calculation is performed in a mid-winter atmospheric model (Fig. 16). The BTD for the mid-winter atmospheric model is smaller than that for the mid-summer atmospheric model. This suggests that the absolute BTD value is effected by cloud temperature and the surface temperature of the earth.

These results indicate that the use of GMS-5 window channels for distinguishing volcanic ash clouds including SiO_2 from ice/water clouds is effective under certain conditions, e.g., cloud containing small particles and appreciable optical depth, but not effective in cases of small optical depth (very thin clouds) or large optical depth (thick clouds).

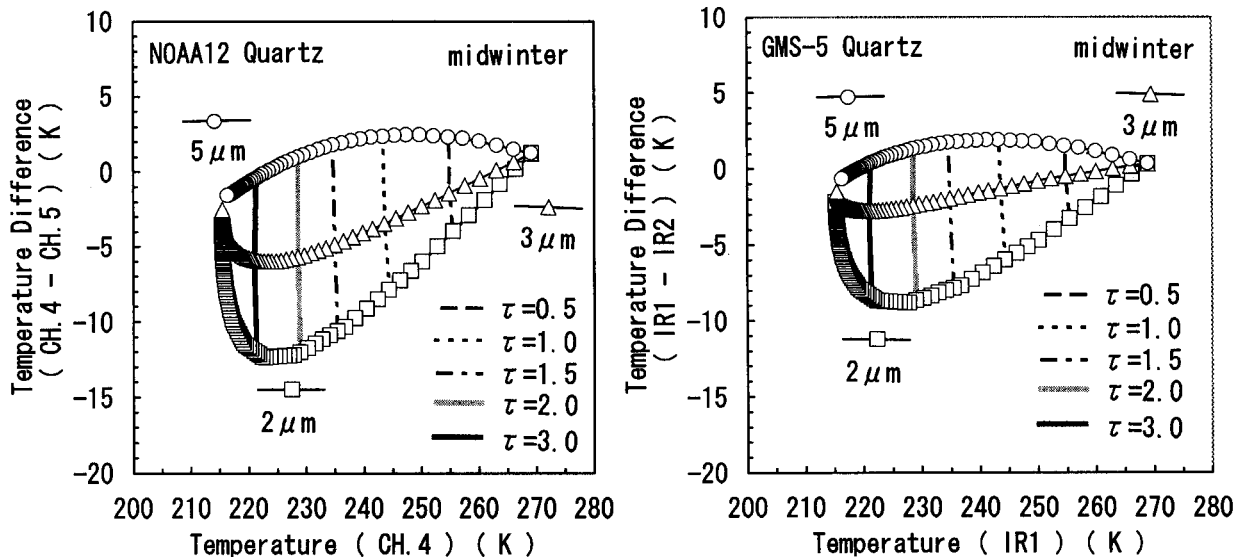


Fig. 16 Same as Fig. 12 except for the mid-winter atmospheric model.

3.4 Mt. Bezymianny Eruption

Mt. Bezymianny (56°58'N, 160°36'E) erupted October 5–6, 1995. VECs from Mt. Bezymianny were observed by GMS-5, NOAA-12, and NOAA-14. We compared VECs from GMS-5 with NOAA-14 because no significant difference exists for spectral response functions of AVHRR channels 4 and 5 between NOAA-12 and NOAA-14 (Fig. 9) for our purposes.

In the GMS-5 VEC IR1 image taken at 0230 UTC Oct. 6, 1995 (Fig. 17), the VECs indicated by the 'a' was characterized as colder than land and sea areas and its colder part was dispersed east. It is very difficult, however, to distinguish the VEC from neighboring ice/water clouds because no significant IR temperature difference occurs between them if there is no eruption.

Fig. 18 shows a series of GMS-5 BTD images together with the NOAA-14 BTD image in the region enclosed in line (A) (Fig. 17) from BTD images taken from 0230 UTC to 0330 UTC Oct. 6, 1995. In Fig. 18, the area with a negative value less than -0.5°C is colored, contrasting with the colorless area with a BTD value exceeding -0.5°C .

As expected, volcanic ash clouds are depicted where the BTD is less than -0.5°C , although the

BTD image of NOAA-14 is clearer than that of GMS-5 due to horizontal and temperature resolution differences and some overlap in the spectral response functions for GMS-5 window channels.

To examine the relationship between BTD and TBB for volcanic ash cloud, we compared BTD with TBB of channel 4 and IR1 for the area enclosed in line (B) (Fig. 17) from images taken at 0230 UTC for GMS-5 and 0250 UTC for NOAA-14 Oct. 6, 1995. Fig. 19 shows scatterdiagram of BTD vs. TBB. The results in Fig. 19 are similar to those for quartz, volcanic dust, and ice in Section 3.3.

In a reference IR image (Fig. 17), positive pixels in Fig. 19 correspond to cirrus area west from the volcano, while negative pixels in Fig. 19 correspond to volcanic ash cloud. The figure also indicates that the volcanic ash cloud is composed of mainly SiO_2 and dust with several sizes of particle (Section 3.3). In addition, the BTD value of GMS-5 is smaller than that of NOAA-14 as shown in the model calculation.

Thus, results obtained in GMS-5 and NOAA-14 observation for the Mt. Bezymianny eruptions agree well qualitatively with results from results calculated by a radiative transfer model.

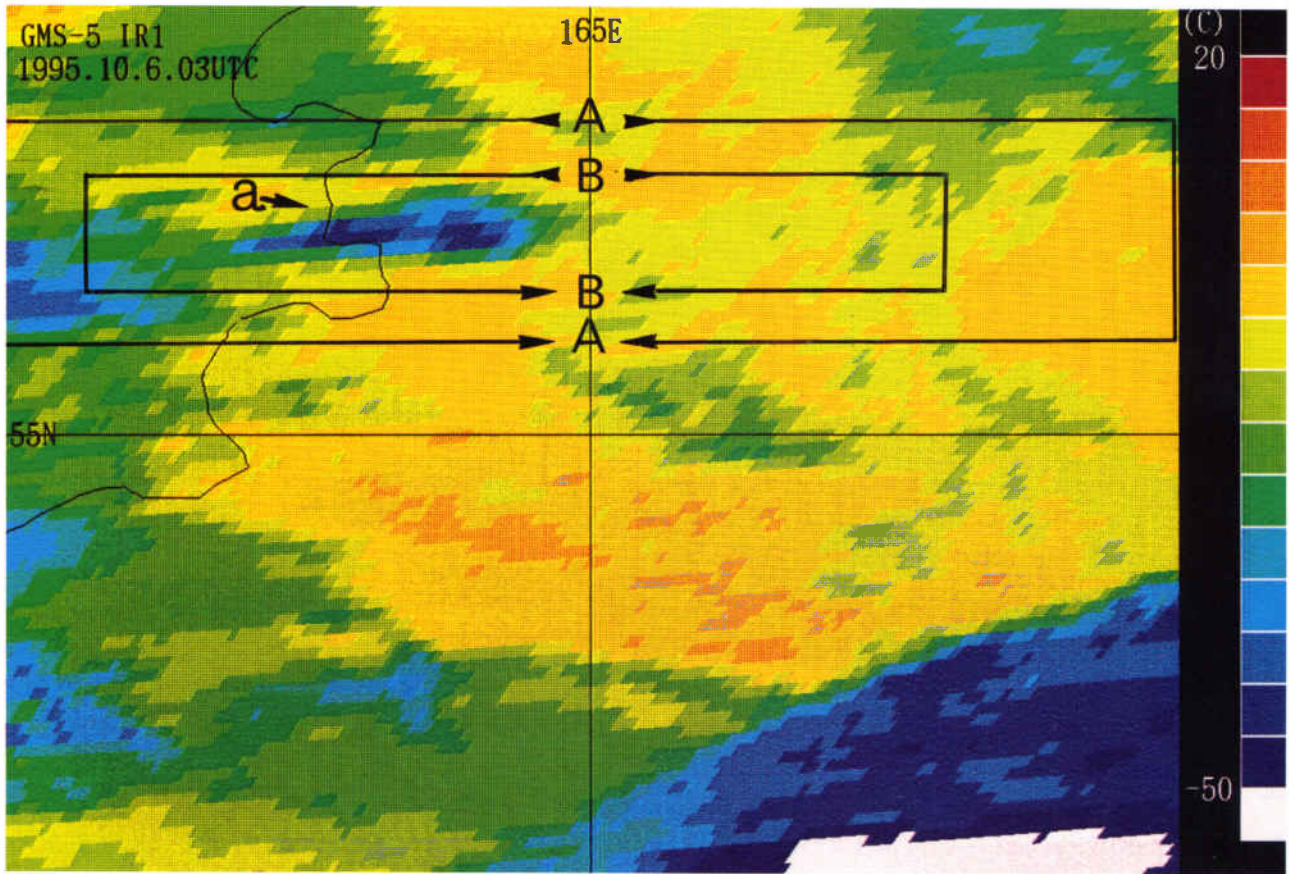


Fig. 17 GMS-5 VEC IR1 image taken at 0230 UTC Oct. 6, 1995. The VECs from Mt. Bezymianny is indicated by the 'a'.

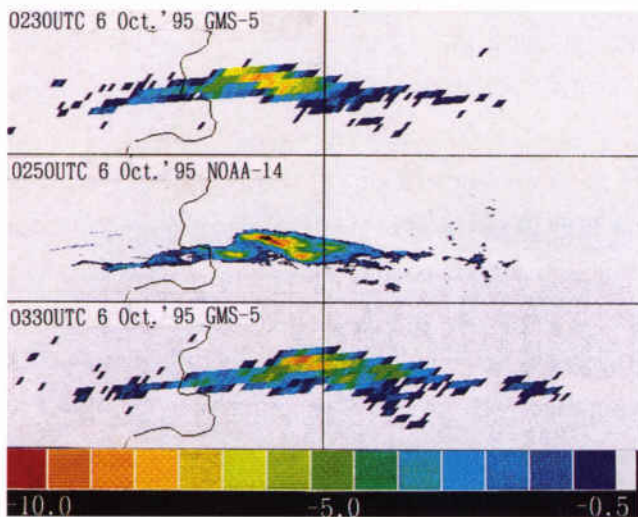


Fig. 18 A series of GMS-5 BTD images together with the NOAA-14 BTD image in the region enclosed in line (A) (Fig. 17) from BTD images from 0230 UTC to 0330 UTC Oct. 6, 1995.

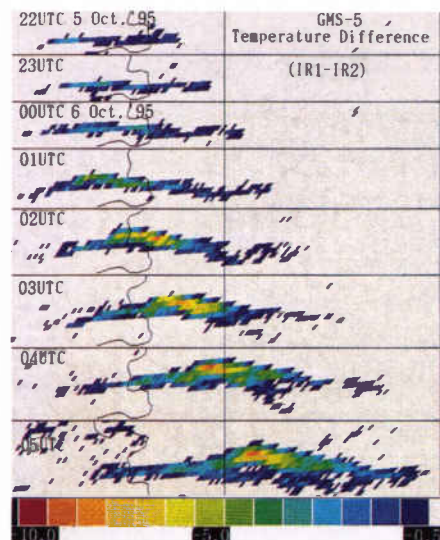


Fig. 20 A series of GMS-5 BTD images from 2130 UTC Oct. 5 to 0430 UTC Oct. 6, 1995 at 1-hr intervals.

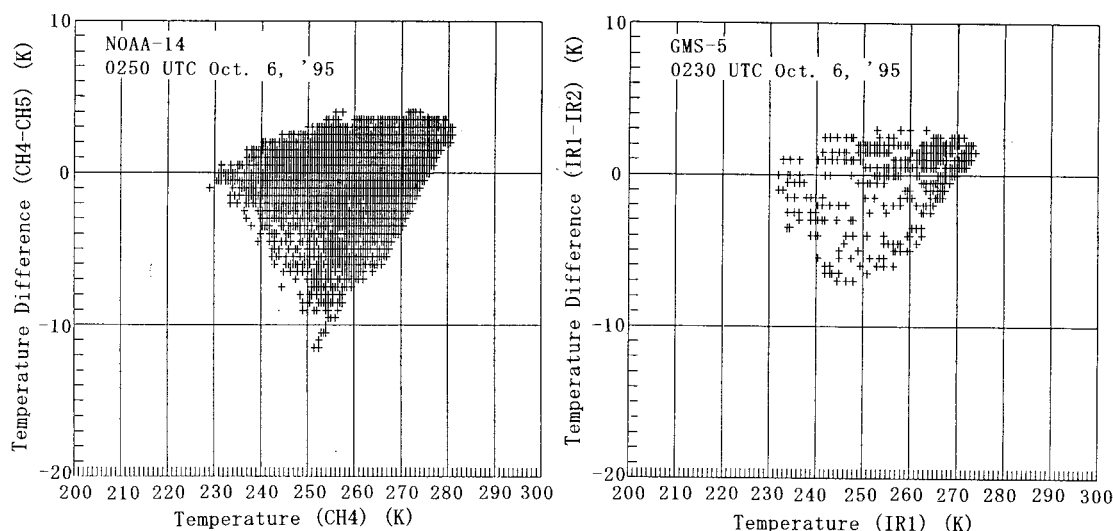


Fig. 19 Observed temperature pairs, BTD of GMS-5 or NOAA-14 AVHRR and IR-1 temperature of GMS-5 or channel 4 temperature of NOAA-14 AVHRR for the area enclosed in line (B) (Fig. 17).

4. Conclusion

GMS-5 infrared data was digitized to only eight bits and some overlap occurred in spectral response functions for the GMS-5 infrared sensors, IR1 and IR2. This led to a reduced BTD for GMS-5 compared to that for NOAA AVHRR.

The effectiveness of GMS-5 window channels, IR1 and IR2, however, in distinguishing volcanic ash clouds as effectively as NOAA AVHRR data is recognized in some circumstances by a radiative transfer model and results in GMS-5 and NOAA-14 observation for the Mt. Bezymianny eruptions. In addition, GMS-5 BTD images are available at hourly intervals, enabling hourly monitoring of volcanic ash cloud (Fig. 20).

Thus, GMS data can help improve volcanic ash cloud warning services.

The next geostationary meteorological satellite (MTSAT) to be launched by Japan is scheduled for 1999. This satellite will have one visible sensor (0.55–0.8 μm) and four infrared sensors (IR1: 10.3–11.3 μm ; IR2: 11.5–12.5 μm ; IR3: 6.5–7.0 μm ; IR4: 3.5–4.0 μm). Infrared data will be digitized to 10 bits, significantly improving the thermal resolution. This satellite will thus further improve detection

and monitoring of volcanic ash clouds.

Reference

- Ackerman, T.P., K.N. Liou, F.P.J. Valero and L. Pfister (1988): Heating rates in tropical anvils, *J. Atmos. Sci.*, 45, 1606–1623.
- Dave, J.V. (1968): Subroutines for computing the parameters of the electromagnetic radiation scattered by a sphere, IBM Palo Alto Scientific Center, 60 pp.
- Funada, H. and K. Arai (1983): GMS-2 observation of volcanic ashes from Mexican volcano El Chichon, Meteorological Satellite Center Technical Note, 7, 13–27 (in Japanese with English abstract).
- Irvine, W.M. and J.B. Pollack (1968): Infrared optical properties of water and ice spheres, *Icarus* 8, 324–369.
- Japan Meteorological Agency (JMA) News (1985), 998, 237. (in Japanese)
- Kneizys, F.X. et al. (1983): Atmospheric Transmittance/Radiance: Computer Code LOWTRAN 6, AFGL-TR-83-0187.
- Potts, R.J. (1993): Satellite observations of Mt. Pinatubo ash clouds, *Aust. Met. Mag.*, 42, 59–68.
- Prata, A.J. (1989): Observations of volcanic ash clouds in the 10–12 μm window using AVHRR/2

- data, *Int. J. Remote Sensing*, 10, 751-761.
- Prata, A.J. and I.J. Barton (1994): Detection and discrimination of volcanic ash clouds by infrared radiometry I: Theory, Proceedings of the First Volume, the First Int. Symp. on Volcanic Ash and Aviation Safety, U.S. Geological Survey Bulletin 2047, 305-311. Thomas J. Casadevall(ed).
- Sawada, Y. (1987): Study on analyses of volcanic eruptions based on eruption cloud image data obtained by the geostationary meteorological satellite (GMS), Tech. Rep. Meteorol. Res. Inst., No.22, 335 pp.
- Spitzer, W.G., and Kleinman, D.A. (1961), Infrared lattice bands of quartz, *Phys. Rev.* 121, 1324-1335.
- Takashima, T. and K. Masuda (1987): Emissivities of quartz and Sahara dust powders in the infrared region (7-17 μ m), *Remote Sens. Environ.* 23, 51-63.
- Tokuno, M., M. Matsuda and K. Tsuchiya (1989): Detection of the volcanic ash cloud from satellite IR data, Proceedings of the 9th Japanese Conference on Remote Sensing, 153-156 (in Japanese).
- Tokuno, M. (1991): GMS-4 observations of volcanic eruption clouds from Mt. Pinatubo, Philippines, Meteorological Satellite Center Technical Note, 23, 1-14.
- Volz, F.E. (1973): Infrared optical constants of ammonium sulfate, Sahara dust, volcanic pumice, and flyash, *Appl. Opt.*, 12(3), 564-568.
- Warren, S.G. (1984): Optical constants of ice from the ultraviolet to the microwave, *Appl. Opt.*, 23(8), 1206-1225.

火山灰雲の衛星観測

徳野 正己

この報告は1995年9月18日-21日までオーストラリアのダーウィン市で開催された火山灰の危険に関するアジア・太平洋地域のワークショップで、著者が「火山灰雲の衛星観測」という題で発表した内容に1995年10月5日-6日に発生したベズミアニ火山噴火による火山灰雲の衛星観測の内容を加えたものである。

1985年の桜島火山噴火、1991年のピナツポ火山噴火、1993年のシベルチ火山噴火による火山灰雲を例にとり、GMSの可視、赤外の連続画像及びNOAA衛星のAVHRRの窓領域チャンネル(チャンネル4及び5)画像の火山灰雲を識別する際の有効性が記述されている。更に、放射モデル計算の結果とベズミアニ火山噴火による火山灰雲の衛星観測の結果から、GMS-5の窓領域チャンネル(赤外1及び赤外2)の画像がNOAA衛星のAVHRRの窓領域チャンネル画像と同様に火山灰雲を識別する際に有効であることが示されている。最後にこの報告では、GMS-5のデータが今後火山灰雲に対する情報サービスに更なる改善をもたらすであろうと結論づけている。